Binder-free $LiMn_2O_4$ Nanosheets on Carbon Cloth for Selective Lithium Extraction from Brine via Capacitive Deionization

Guangqiang Ma, Yingsheng Xu, Anjiang Cai,*, Hengjian Mao, Xinyuan Zhang, Dong-Myeong Shin, Lei Wang, and Hongjian Zhou*

G. Ma, Prof. A. Cai, Prof. L. Wang
School of Mechanical and Electrical Engineering, Research Institute of Membrane Separation Technology of Shaanxi Province
Xi'an University of Architecture and Technology
Xi'an 710055, P. R. China
E-mail: cai_aj@163.com

G. Ma, Prof. H. Zhou
Salt Lake Chemical Engineering Research Complex, Qinghai University
Xining 810016, P. R. China
E-mail: hjzhou@issp.ac.cn

G. Ma, Dr. Y. Xu, H. Mao, X. Zhang, Prof. H. Zhou
Key Laboratory of Materials Physics, Centre for Environmental and Energy Nanomaterials, Institute of Solid State Physics
Hefei Institutes of Physical Science, Chinese Academy of Sciences
Hefei 230031, P. R. China
E-mail: hjzhou@issp.ac.cn

H. Mao, X. Zhang, Prof. H. Zhou
Science Island Branch of Graduate School
University of Science and Technology of China
Hefei 230026, P. R. China
E-mail: hjzhou@issp.ac.cn

Prof. D. M. Shin
Department of Mechanical Engineering
The University of Hong Kong
Pokfulam Road, Hong Kong 999077, China

Abstract: In this study, we applied a three-step strategy including electrochemical cathode deposition, self-oxidation, and hydrothermal reaction to prepare the $LiMn_2O_4$ nanosheets on carbon cloth (LMOns@CC) as a binder-free cathode in a hybrid CDI cell for selectively extracting lithium from salt-lake brine. The binder-free LMOns@CC

electrodes were constructed from dozens of 2D $LiMn_2O_4$ nanosheets on carbon cloth substrates, resulting in a uniform two-dimensional array of highly ordered nanosheets with hierarchical nanostructure. The charge/discharge process of the LMOns@CC electrode demonstrated that visible redox peaks and high pseudocapacitive contribution rates endow the LMOns@CC cathode with a maximum Li^+ ion electrosorption capacity of 4.71 mmol g^{-1} at 1.2 V. Moreover, the LMOns@CC electrode performed outstanding cycling stability with a high-capacity retention rate of 97.4% and a manganese mass dissolution rate of 0.35% over ten absorption-desorption cycles. The DFT theoretical calculations verified that the Li^+ selectivity of the LMOns@CC electrode is attributed to the greater adsorption energy of Li^+ ions than other ions. Finally, the selective extraction performance of Li^+ ions in natural Tibet salt lake brine revealed that the LMOns@CC has selectivity ($\alpha_{Mg^{2+}}^{Li^+} = 7.48$) and excellent cycling stability (100 cycles), which would make it a candidate electrode for lithium extraction from salt lakes.

Keywords: Capacitive deionization, $LiMn_2O_4$, Lithium extraction, Binder-free electrode, Selective electrosorption.

1. Introduction

As the lightest metallic element in nature, lithium is an important strategic resource in electric vehicles, aviation, 3C products, mobile devices, and ceramic materials, so it has been praised as the "21st-century energy metal".[1, 2] The worldwide supply of lithium ore is gradually declining and can no longer satisfy market demand as the pace of modernization and the rising need for lithium resources globally. The annual Li

consumption rate in the world will continue to increase from 2023 to 2050, and it is expected to consume more than a third of the total lithium reserves on land.[3-5] In comparison to lithium ore, seawater and brine have a substantially higher overall lithium resource content.[6, 7] Additionally, the commercial approach to lithium recovery from lithium ore has some defects, including high cost, convoluted procedure, and the release of potentially harmful compounds into the environment. Therefore, it is crucial to extract lithium from seawater and brine to resolve this conflict.[8] Despite this, a significant portion of lithium resources in China are extracted from the brines of salt lakes, which have very high Mg/Li ratios, but at a high cost because Li/Mg separation is challenging. The breakthrough of selective lithium extraction technology from seawater or brine solutions can effectively alleviate the shortage of lithium resources.

Currently, many technologies have been applied to Li^+ extraction from brine, including precipitation,[9-11] solvent extraction,[12-14] electrochemical recovery,[15-17] and membrane separation.[18-21] However, these techniques usually exist some issues, for instance, low selectivity, cumbersome operations, long production periods, or high energy consumption. Furthermore, the co-existence of the cations (Na^+, K^+, Ca^{2+}, Mg^{2+}, etc.) in the brine makes it considerably harder to extract Li^+. Therefore, it is imperative to use an efficient method for the high-efficiency selective extraction of Li^+ ions from brine. Recently, lithium has been selectively extracted from brine by using capacitive deionization (CDI), which is a developing desalination technology with low cell voltage, high energy efficiency, and environmental friendliness.[22] Similar to the principle of ion storage in supercapacitors, the CDI cell applies a certain electric field between the

two electrode plates. Under the action of the electric field force, the charged ions are adsorbed on the electrode surface due to the principle of opposite-charge attraction. When the reverse electric field or the short circuit is applied, the ions adsorbed on the electrode are released to ensure the *in-situ* regeneration of the CDI electrode. The application of CDI technology in Li^+ extraction from brine mainly focuses on Li^+-ion sieve materials, including λ-MnO_2,[22] $Li_{1.6}Mn_{1.6}O_4$,[23] $LiMn_2O_4$,[24] and other titanium- or iron-based oxides.[25-27] Among them, spinel $LiMn_2O_4$ (LMO) has been widely used for electrochemical Li^+ extraction because of its affordability, ease of preparation, and eco-friendliness.[28] However, the main drawbacks of LMO include instability (manganese dissolution) and inadequate rate capacity (low conductivity of 10^{-6} S cm^{-1}), which greatly restrict its practical application.[29]

To address these issues, modification and doping strategies were developed to solve the inherent defects of LMO electrodes. For instance, Shang *et al.*[30] realized selective Li^+ extraction by doping Ni in the LMO structure, in which the maximum adsorption capacity is 260 μmol g^{-1}, and the dissolution rate of manganese is 7% after 20 cycles. Wang *et al.*[23] reduced the dissolution of manganese and enhanced the electrical conductivity of LMO electrodes by designing a carbon-coated core-shell structure, delivering a remarkable capacity of 9.45 mmol g^{-1} with a low manganese dissolution rate of 7.5% after ten cycles. Shang *et al.*[31] improved the electrical conductivity and cycling stability of LMO by stringing the LMO particles with multi-walled carbon nanotubes to form a net-like structure, in which the area resistance was reduced to 156.2 Ω cm^{-2}, the capacity remained above 90% even after 100 cycles, and

the dissolution of manganese is almost inappreciable. Above all, two key issues remain: (i) The majority of the work concentrates on the modification of LMO particles or powder, in which the low specific surface area and inferior exposure of active sites are their inherent features; (ii) The use of binders leads to decreased electronic conductivity, terrible cycling stability, and inferior specific capacities of LMO electrodes because of the insulation and electrochemical inactivity of the binder.

Therefore, it is feasible to construct the binder-free electrodes by *on-site* growth of the objective materials with highly ordered hierarchical nanostructures on a flexible conductive carbon cloth substrate. This strategy can effectively build a superior three-dimensional conductive network for adequate electron transformation, more vitally avoiding the attenuation of electrochemical properties derived from the failure of the binder. Recently, the reported customized hierarchical nanostructures have been shown to significantly enhance the integral structural stability and ion/charge transfer rate during the electrochemical process. For example, a combined and unsupported SnS_2 nanosheets@graphite paper electrode were superior to those of the pristine SnS_2 power in terms of high desalination capacity, good reaction rate, and amazing cycle ability.[32] In addition, the application of graphene nanostructures@Ni foam,[33] VS_2 nanosheets@graphite paper,[34] and MXene/CNT[35] also demonstrated the advantages of integrated binder-free electrodes with hierarchical nanostructures for capacitive deionization.

In this work, a feasible three-step strategy to fabricate binder-free $LiMn_2O_4$ nanosheets (LMOns) electrodes on carbon cloth (CC) substrates was proposed for

selective extraction of lithium from salt lake brine: (i) Firstly, $Mn(OH)_2$ nanosheets were grown *in-situ* on a carbon cloth substrate by the electrodeposition method; (ii) Secondly, $Mn(OH)_2$ nanosheets were easily oxidized to Mn_3O_4 under ambient temperature; (iii) Finally, the "spinel-to-spinel" Mn_3O_4 was lithiated into LMO through a one-step hydrothermal reaction. The binder-free LMOns@CC electrodes could have high-performance Li^+ extraction from brine, benefiting from their high exposure to activated sites, greater variable specific capacity, and excellent cycle stability. Meanwhile, the structure, morphology, and electroactivity of the LMOns@CC electrode were characterized by SEM, TEM, XRD, XPS, and electrochemical tests. In addition, the prominent selectivity coefficient of Li^+ extraction was obtained in a lab-made solution with a high Mg/Li molar ratio and a natural Tibet salt lake brine. The selective electrosorption mechanism of the LMOns@CC electrode was further explained by DFT theoretical calculation. This research offers a fresh viewpoint on the practical design of LMO electrodes for future Li^+ extraction from brine.

2. Results and discussion

2.1. Characterization of the binder-free LMOns@CC electrodes

The synthesis process of the binder-free LMOns@CC electrode is illustrated in **Figure 1**. Firstly, *in-situ* cathodic deposition of $Mn(OH)_2$ on the CC substrates was implemented in an electrochemical three-electrode system by using hydrogen bubbles as a soft template. Divalent manganese (E° = -0.828 V vs. normal hydrogen electrode

(NHE)) has a reduction potential that is more negative than that of hydrogen (E° = -1.180 V vs. NHE).[36] Therefore, hydrogen would be generated first when the voltage of the working electrode is -1.4 V. During the reaction, hydrogen bubbles are formed on the cathode surface due to the electrolysis of water, which increases the concentration of OH^- near it. Uniform precipitation particles rather than the 2D mesoporous nanosheet with the hierarchical structure are generated on the substrate if there is no continuous formation of H_2 bubbles as a dynamic template. Moreover, the excess hydroxide ions continuously interacted with manganese ions in the electrolyte to form a 2D hierarchical $Mn(OH)_2$ nanosheet array by continuously stacking the nanoparticles due to the precipitation along H_2 bubbles. Subsequently, $Mn(OH)_2$ was easily oxidized to form Mn_3O_4 after regular drying at ambient temperature, which is attributed to its extreme instability in the presence of oxygen. Finally, the lithiation of Mn_3O_4 into LMO was performed through a one-step hydrothermal reaction. The nanosheet morphology was retained in the whole synthesis process, in which no binder was used. The color comparison photographs before and after the sample are shown in **Figure S3**. The carbon cloth changes from black at the beginning to yellow for Mn_3O_4 and finally becomes black again as the formation of LMOns.

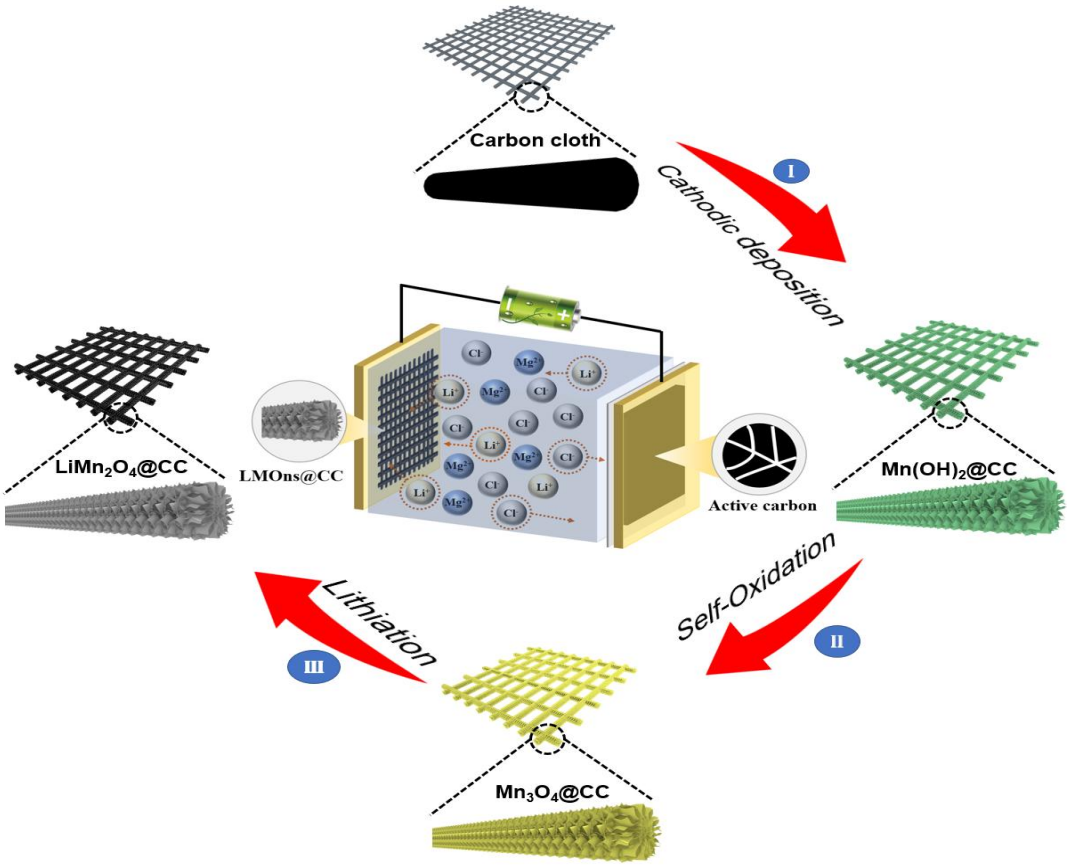

Figure 1. Illustration for the fabrication of binder-free $LiMn_2O_4$ nanosheets on carbon cloth substrates.

Figure 2a–c depicts SEM images of Mn_3O_4 nanosheets on the carbon cloth substrates with different magnifications, in which a highly ordered array of nanosheets wraps on the surface of each CC fiber, displaying a mesoporous structure. The multiple interwoven nanocrystallines that make up the nanosheets range in size from 10 to 40 nm in the TEM image of **Figure S4a**. Moreover, each Mn_3O_4 particle has a clear lattice fringe with a plane distance of 0.49 nm, as shown in **Figure S4b**, which is precisely consistent with the (101) plane of the tetrahedron Mn_3O_4. The selected area electron diffraction (SEAD) pattern of Mn_3O_4 nanosheets in **Figure S4c** reveals a polycrystalline structure, in which the characteristics of the diffraction ring can

accurately correspond to the Mn_3O_4 spinel. After hydrothermal lithiation, the Mn_3O_4 was converted to $LiMn_2O_4$ with unchanged nanosheet-like morphology (**Figure 2d-f**). As displayed in **Figure 2c** and **2f**, the thickness of $LiMn_2O_4$ nanosheets is larger than that of Mn_3O_4, demonstrating the volume expansion after the lithium-ion is intercalated into Mn_3O_4. Meanwhile, the surface of $LiMn_2O_4$ nanosheets became rough. It demonstrated that the lithium has interacted with Mn_3O_4 successfully to form the spinel-structured $LiMn_2O_4$ nanosheets, which are constructed from dozens of octahedron-like nanoparticles (inset image of **Figure 2f**). Noteworthy, a nanosheet with a hierarchical structure consisting of nanoscale particles could provide more active sites, shorten the ion transport path, and result in a sizeable pseudocapacitive contribution. The TEM image in **Figure 2g** illustrates that the LMO nanosheets are formed by numerous nanoparticles, which is well consistent with SEM images. The LMOns have a width of about 1.2 μm and a thickness of about 63.5 nm. **Figure 2h** shows a distinct lattice fringe with an interplanar spacing of 0.48 nm, which is corresponding to the (111) plane of spinel $LiMn_2O_4$ (JCPDS card. 35-0782). Five bright diffraction rings corresponding to the (111), (311), (400), (511), and (440) planes of $LiMn_2O_4$ were observed from the SEAD pattern (**Figure 2i**), indicating that the highly ordered array of LMO nanosheets features a high degree of crystallinity.

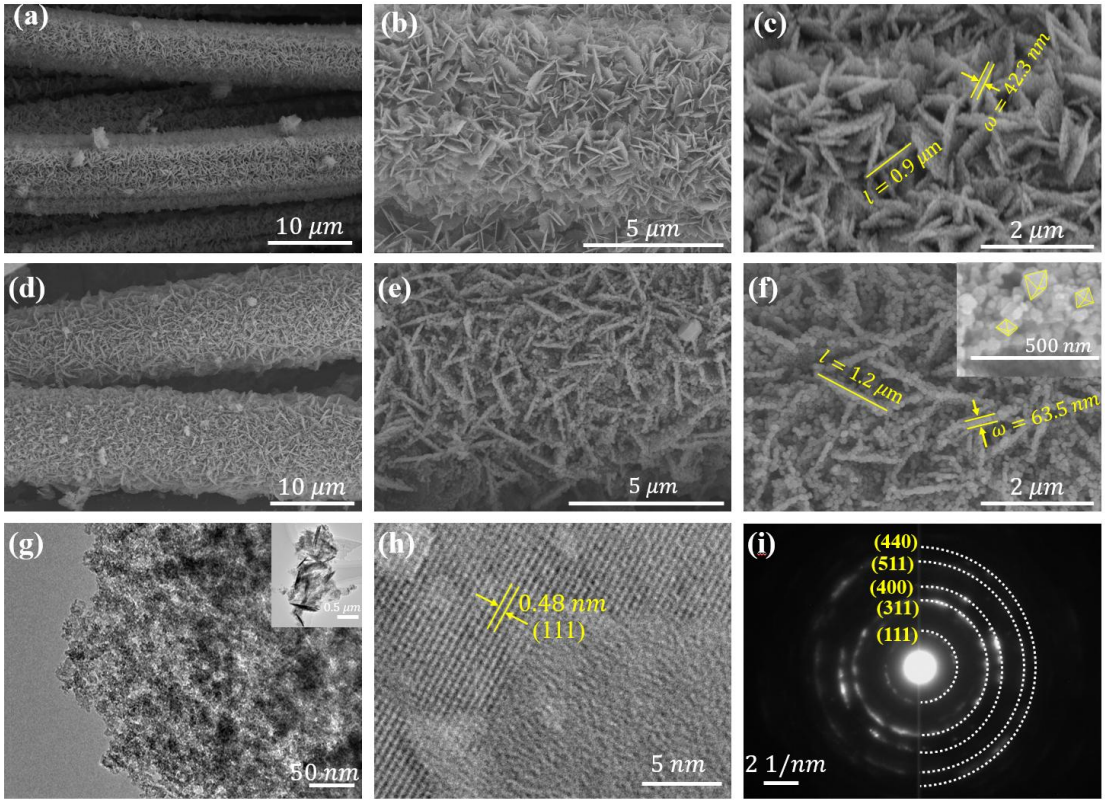

Figure 2. a-c) SEM images of Mn_3O_4 nanosheets; d-f) SEM images of $LiMn_2O_4$ nanosheets; g-h) TEM images of $LiMn_2O_4$ nanosheets; i) SEAD pattern of $LiMn_2O_4$ nanosheets.

The Mn_3O_4 nanosheets in this study have a mesoporous structure, which both makes it easier to lithiate over a high specific surface area and improves structural stability throughout the phase transition. The rich porous structure of nanosheets allows for bigger volume changes or strains during lithiation, maintaining the fundamental nanosheet architecture. The structural similarities between Mn_3O_4 and $LiMn_2O_4$ may also make the phase transition more seamless and cause less morphological change. **Figure 3a** presents a schematic illustration of the crystal conversion of Mn_3O_4 into $LiMn_2O_4$. The specific reaction process was as follows:

$$8Mn_3O_4 + 12LiOH + 5O_2 \rightarrow 12LiMn_2O_4 + 6H_2O \quad (1)$$

During the hydrothermal reaction, the Mn^{2+} in Mn_3O_4 was oxidized to Mn^{3+} or Mn^{4+}, which is unstable at the tetrahedral sites, and then moved to octahedral sites. Subsequently, the inserted Li^+ occupies the remaining vacancies to form spinel $LiMn_2O_4$. The XRD patterns also demonstrated that the intermediate state of Mn_3O_4 is transformed into a $LiMn_2O_4$ phase with a high crystallinity (**Figure 3b**). On the other hand, no diffraction peak of Mn_3O_4 was found in the XRD pattern of $LiMn_2O_4$, indicating the successful synthesis of pure $LiMn_2O_4$ during the hydrothermal reaction process.

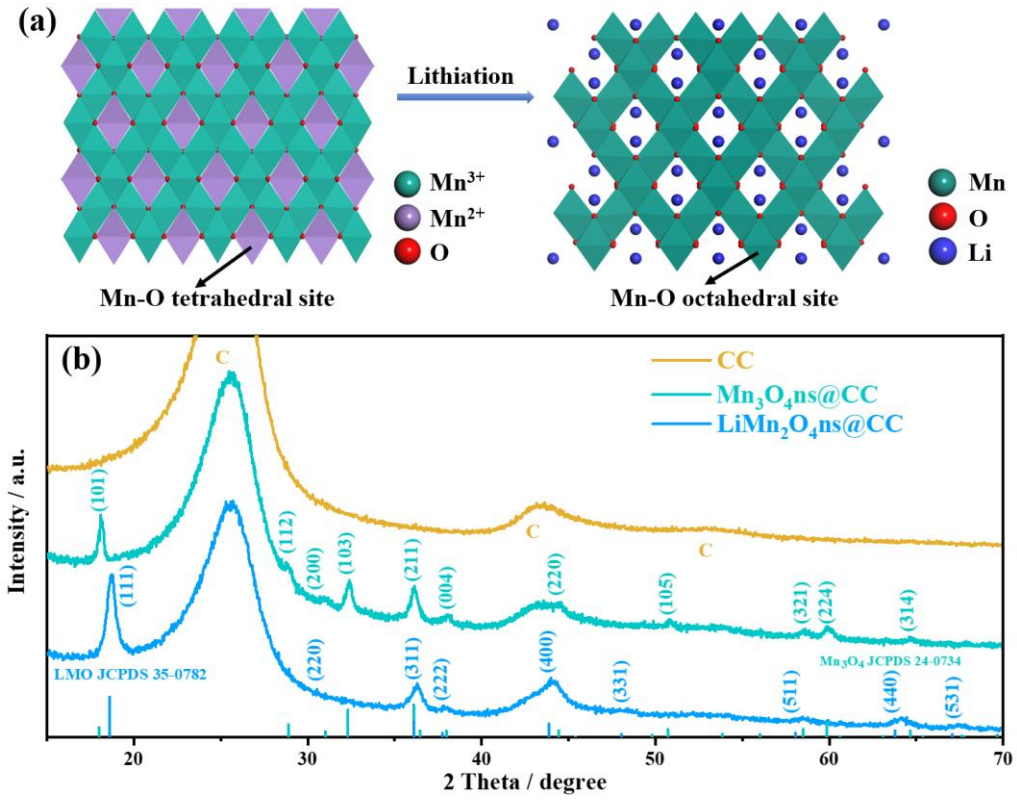

Figure 3. a) Schematic illustration for crystal conversion of Mn_3O_4 into $LiMn_2O_4$; b) XRD patterns of Mn_3O_4 nanosheets and $LiMn_2O_4$ nanosheets on the carbon cloth substrates.

3.2 Electrochemical performance of binder-free LMOns@CC electrode

To evaluate the electrochemical performance of binder-free LMOns@CC electrode, a three-electrode electrochemical system was carried out in an electrolyte of 0.5 M LiCl. The CV curves of the LMOns@CC electrode were displayed in **Figure 4a** for various scan rates (0.1-1 mV s^{-1}) within a voltage range of 0.4-1.1 V. The two pairs of redox peaks originated from the typical feature of pseudocapacitive $LiMn_2O_4$ materials, which were distinctly observed at each scan rate, exhibiting fast Li^+ (de)intercalation and excellent rate capability. The deintercalation behavior of Li^+ ions can be divided into two continuous reactions. The first step is the deintercalation of 0.5 Li^+ ions at nearly 0.75 V (peak 1) in the anode direction corresponding to reaction (2), and the other 0.5 Li^+ ions are deintercalated at 0.91 V (peak 2) during the second step corresponding to reaction (3). Correspondingly, the intercalation of Li^+ ions also consists of two processes at ca. 0.86 V and 0.68 V in the cathode direction, corresponding to peak 3 and peak 4 of the CV curves in **Figure 4a**, respectively. The detailed reactions were as follows:

$$LiMn_2O_4 - 0.5e^- - 0.5Li \rightleftharpoons Li_{0.5}Mn_2O_4 \quad (2)$$

$$Li_{0.5}Mn_2O_4 - 0.5e^- - 0.5Li \rightleftharpoons \lambda\text{-}MnO_2 \quad (3)$$

Figure 4b also shows the GCD curves for the LMOns@CC electrode at various current densities. All the GCD curves appeared as two apparent platforms at various current densities, indicating the characteristic pseudocapacitive behavior of the LMOns@CC electrode for the electrosorption of Li^+ ions, which precisely matches with

the redox potential of CV.

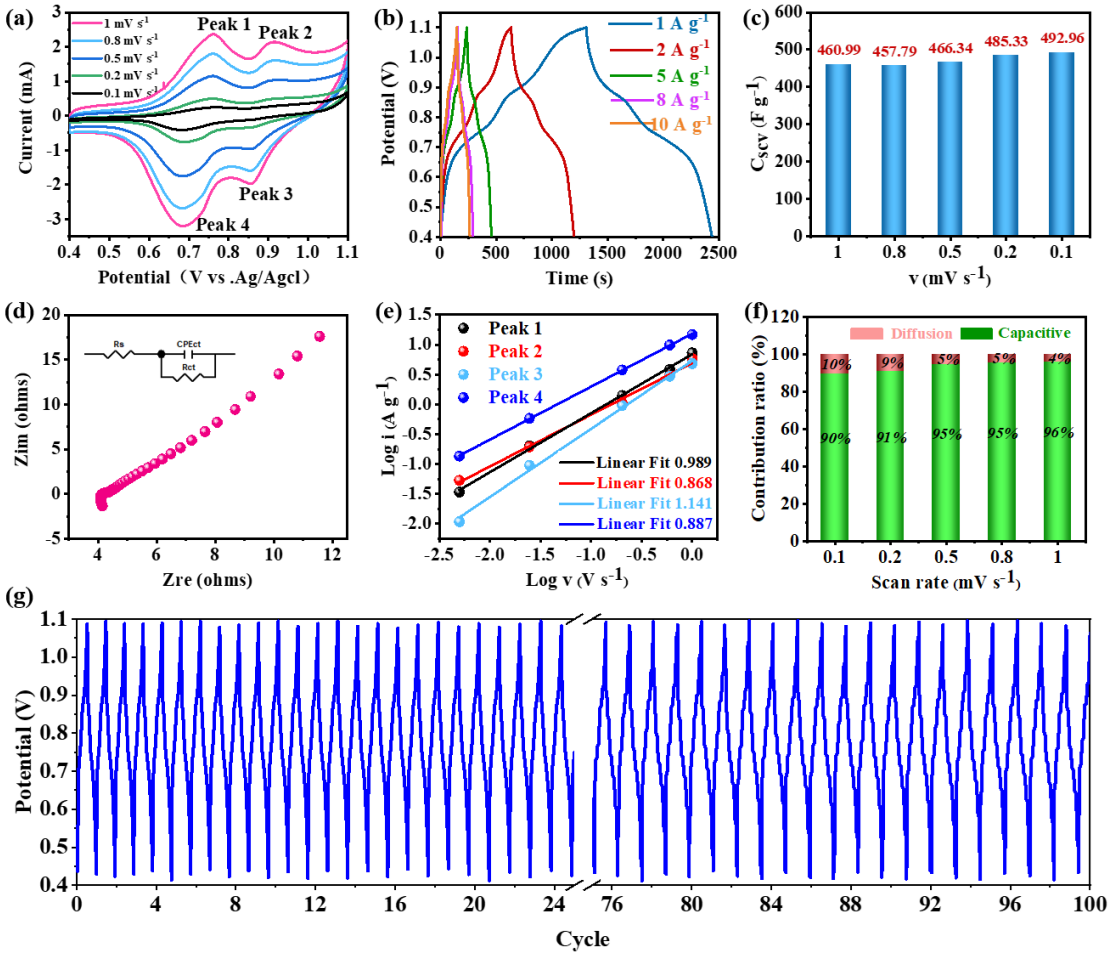

Figure 4. a) Cyclic voltametric curves of the LMOns@CC electrode at various scan rates of 0.1–1 mV s^{-1}; b) GCD curves of the LMOns@CC electrode at various current densities of 1–10 A g^{-1}; c) Specific capacitance of the LMOns@CC electrode at various scan rates based on the CV curves; d) EIS plot of the LMOns@CC electrode measured at 0.378 V vs. SCE and their Randles equivalent circuit. e) Log (peak current, I_p) vs. log (scan rate, v) plots of the LMOns@CC electrode according to anodic and cathodic peaks in CV curves; f) Contribution ratios of the capacitive and diffusion-controlled processes at various scan rates for the LMOns@CC electrode; g) 100 cycles of GCD curves for the LMOns@CC electrode at 5 A g^{-1}.

Figure 4c shows the specific capacitance of the LMOns@CC electrode calculated by Equation 1 at various scan rates, up to 493.0 F g^{-1}, which is close to the theoretical specific capacitance (532.8 F g^{-1}) of LMO.[37] This is attributed to the fact that the LMOns@CC electrode is composed of countless small particles and has a high crystallinity and porous structure, thus providing abundant active sites. **Figure 4d** displays EIS plot of the LMOns@CC electrode under the open circuit. A small charge transfer resistance in the high-frequency region and a line with a nearly 45° slope in the low-frequency region indicated the fast ion diffusion in the LMOns@CC electrode, which is conducive to the electrosorption of Li^+ ions. It further demonstrated that the high ordered array binder-free LMO nanosheet shortens the transport distance of lithium ion on the electrode. The Randles equivalent circuit was displayed in the inset image of **Figure 4d**, in which R_s is 4.15 Ω and the diffusion coefficient is 8.32×10^{-12} cm^2 s^{-1}. The results show that the LMOns@CC electrode has a higher diffusion coefficient, indicating a higher extraction efficiency of the electrode in lithium extraction from the salt lake. To understand the Li^+ ion storage mechanism, the Bruce Dunn typical theory was introduced as the following power law relation:

$$i(v) = av^b \quad (4)$$

where *I* indicates current, *V* represents the sweep speed; *a* and *b* are constants. Generally, one *b* value of 0.5 represents the complete diffusion control process, and one *b* value of 1.0 reveals the surface capacitance control process. According to the systematical calculation, the *b* values at diverse cathodic and anode peaks were 0.989 (peak 1), 0.868

(peak 2), 1.141 (peak 3), and 0.887 (peak 4), respectively (**Figure 4e**). This result indicated that the (de)intercalation of Li^+ ions is mainly the capacitive-controlled behavior process. The contribution ratios of the two parts can be calculated or divided by the formula $i(v) = k_1 + k_2 v^{1/2}$ according to previous work.[38, 39] **Figure 4f** shows the different capacitive contribution ratios of 90%, 91%, 95%, 95%, and 96% between 0.1 and 1.0 mV s^{-1}. The high surface capacitance ratio could significantly improve the electrosorption performance of the LMOns@CC electrodes during the HCDI process.

In brief, the highly ordered array of binder-free LMO nanosheets can effectively shorten the charge transfer path, and thus reduce the internal resistance. Mesoporous nanosheets composed of countless nanoparticles with many active sites can significantly improve the electrosorption performance of Li^+ ions. Finally, the 100-cycle GCD curve of the electrode at 5 A g^{-1} current density in **Figure 4g** shows good cyclic stability of the LMOns@CC electrode with a retention rate of 97.6%. This is due to the strong structural stability, high crystallinity, and the formation of a surface that inhibits the dissolution of manganese.

3.3 HCDI performance of the binder-free LMOns@CC electrode

The HCDI performance of the LMOns@CC electrode was investigated in different Li^+ ion-contained solutions under a batch mode. An HCDI cell (LMOns@CC//AC) containing a pretreated LMO cathode electrode (L_{1-x}MOns@CC) and an AC anode electrode was assembled to explore the selective extraction of Li^+ ions. The mass fraction of pre-desorbed lithium accounts for 60% of the total mass according to the ICP-AES measurement, which is conducive to maintaining the structural stability of

the LMO material, so as to give full play to the optimal performance without damaging the crystal structure in the process of Li^+ ion intercalation and deintercalation (**Figure S5**).[40] Due to the pre-desorption of Li^+ ions, the lattice of the LMOns@CC electrode shrunk, resulting in the overall diffraction peaks will shift to a higher angle (**Figure S6**). The HCDI performance was studied by assembling the HCDI structure with a couple of electrodes (LMOns@CC as the cathode and AC as the anode), as shown in **Figure 5a.** To eliminate the interference of carbon cloth substrate, moreover, the adsorption-desorption experiment of pure CC on Li^+ ions was firstly performed before the electrosorption of LMOns@CC electrode. **Figure S7** shows that the pure carbon cloth substrate has an ignorable adsorption effect at 1.2 V, excluding the influence of pure CC in subsequent experiments. **Figure 5b** exhibits an overall adsorption-desorption process of Li^+ ions for the LMOns@CC electrode. It is worth noting that the electrosorption process of Li^+ ions are speedy, reaching 93.5% of the maximum electrosorption capacity (4.71 mmol g^{-1}) in 15 minutes. This is because that the LMOns@CC electrode has more active sites and unuse of a binder in comparison with traditional $LiMn_2O_4$ electrodes. **Figure 5c** shows the electrosorption capacity curves of the LMOns@CC electrode at different initial Li^+ concentrations under 1.2 V. As a result, the electrosorption capacity of the LMOns@CC electrode also gradually rises with the increase in Li^+ ion concentration, which is attributed to the higher ionic strength producing a more vital driving force. The maximum Li^+ electrosorption capacity was 4.71 mmol g^{-1} at the ion concentration of 200 mg L^{-1}. As illustrated in **Figure 5d**, the influence of the voltages on the electrosorption performance of the LMOns@CC

electrode at Li^+ ions concentration of 200 mg L^{-1} was also investigated. The electrosorption capacity of LMOns@CC electrode at 60 minutes steadily increased from 3.82 mmol g^{-1} at 0.8 V to the highest value of 4.71 mmol g^{-1} at 1.2 V. This increment in electrosorption capacity results from the more potent interaction force between Li^+ ions and electrodes at higher applied voltages. To avoid side reactions, including water electrolysis, chlorine oxidation, and material dissolution, the applied voltage exceeding 1.2 V was not considered. The electrosorption capacity and electrosorption rate of the LMOns@CC electrodes were also determined by using the Kim-Yoon plot. Generally, the shift of Kim-Yoon plot to the top right corner manifests a strong electrosorption capacity and quick electrosorption rates. **Figure 5e** illustrates the Kim-Yoon plot of the LMOns@CC electrodes at different applied voltages. It can be clearly seen that the electrosorption capacity and electrosorption rate gradually increase with the rise of applied voltage, which is due to the increase of electrosorption capacity caused by the continuous enhancement of the electric field force. The corresponding maximum electrosorption rate were 0.97 (1.2 V), 0.55 (1.0 V), and 0.48 (0.8 V) $mmol \cdot g^{-1} \cdot min^{-1}$, respectively. Furthermore, the electrosorption capacity of our proposed binder-free LMOns@CC electrode is superior to those of the reported LMO electrodes in previous works,[41-46] indicating the integrated advantages of binder-free and a uniform two-dimensional array of highly ordered nanosheets with hierarchical nanostructure (**Figure 5f**).

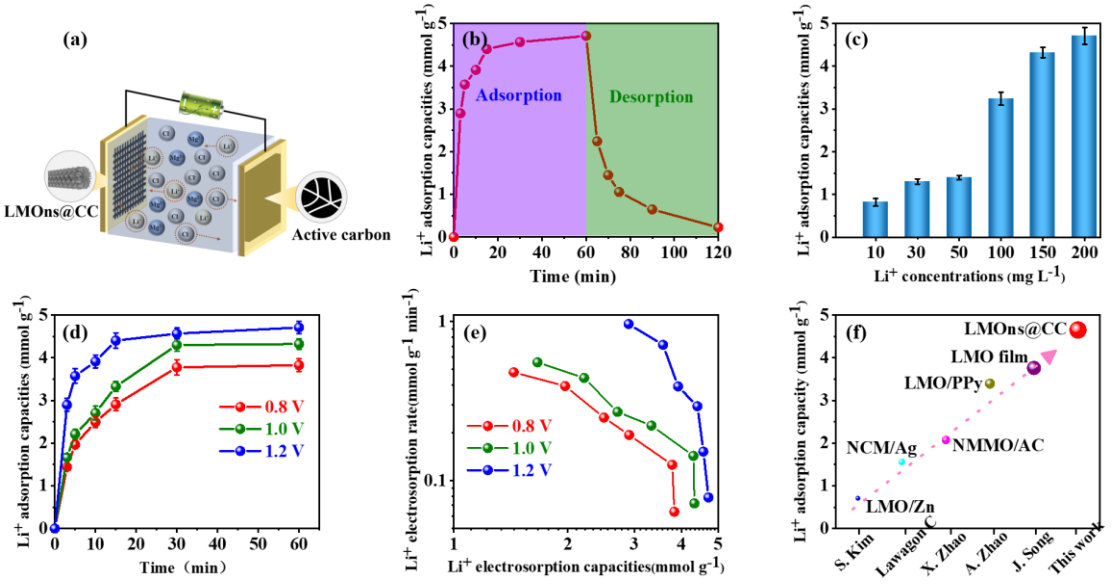

Figure 5. a) Schematic diagram of hybrid capacitive deionization (LMOns@CC||AC); b) Electrosorption-desorption curve of the LMOns@CC electrode in 200 mg L^{-1} of Li^+ ions solution at 1.2 V and flow velocity of 15 mL min^{-1}; c) Electrosorption capacity of the LMOns@CC electrode under the different concentrations of Li^+ ions solution at 1.2 V; d) Electrosorption capacity of the LMOns@CC electrode at different voltages in 200 mg L^{-1} of Li^+ ions solution; e) Corresponding Kim-Yoon plot of the LMOns@CC electrode at different voltages in 200 mg L^{-1} of Li^+ ions solution; f) Comparison of the adsorption capability with the other reported LMO electrodes in previous works.

In order to reveal the electrochemical intercalation/deintercalation processes of Li^+ ions, the *ex-situ* XPS spectra of the LMOns@CC electrodes were measured before and after Li^+ ions electrosorption. As illustrated in **Figure 6a**, the Mn $2p_{3/2}$ peak and the Mn $2p_{1/2}$ peak of LMOns@CC divide into Mn^{3+} peaks and Mn^{4+} peaks equally for the lithium intercalation state (LMOns@CC). For the lithium deintercalation state (L_{1-x}MOns@CC) in **Figure 6b**, the Mn $2p_{3/2}$ and Mn $2p_{1/2}$ peaks of L_{1-x}MOns@CC were

occupied mainly by Mn^{4+} peaks, while the Mn^{3+} peaks only occupied a smaller portion. The redox reactions of Mn^{3+}/Mn^{4+} certainly occurred in the LMOns@CC electrode during intercalation and deintercalation of Li^+ ions, which is an apparent correspondence with the XRD pattern of the LMOns@CC electrode in **Figure 6c**. During the desorption process, the diffraction peaks at 18.61° of the LMOns@CC electrodes shifted to a higher angle (18.97°) due to the lattice shrinkage of the LMOns@CC electrodes in the deintercalation of Li^+ ions. Notably, during the adsorption-desorption process, the C-peak does not have any deviation, confirming that the entire process is the deintercalation of ions rather than the interference of other factors. Moreover, the entire XRD characteristic peaks restore to the original state after the intercalation of Li^+ ions during CDI electrosorption. It proved that the Li^+ intercalation/deintercalation based on the reversible reaction in the LMOns@CC electrodes could be achieved by the electrosorption-desorption process of HCDI, suggesting potentially considerable cyclable capability of LMOns@CC electrodes.

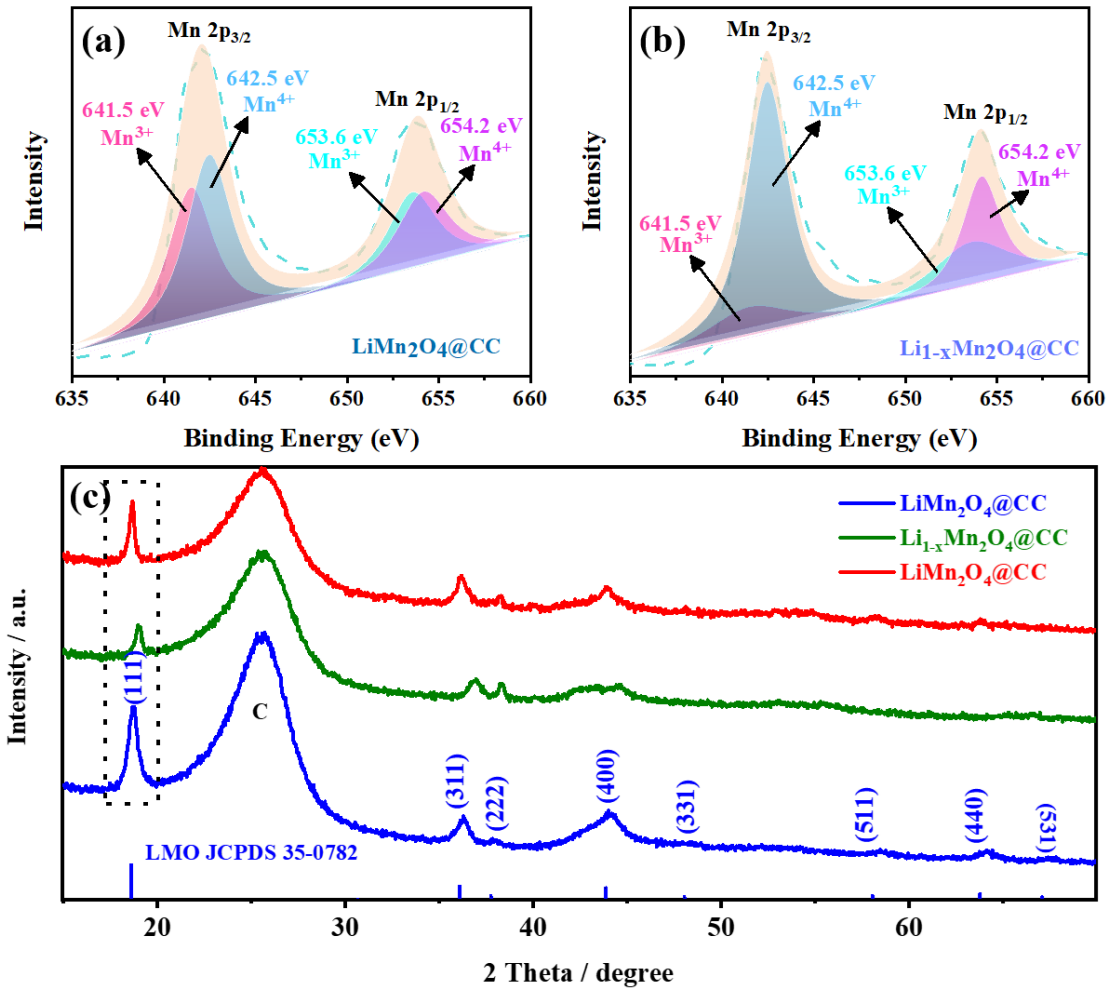

Figure 6. a) *Ex-situ* X-ray photoelectron spectroscopy (XPS) of LMOns@CC; b) *Ex-situ* XPS spectrum of L_{1-x}MOns@CC; c) Comparison of XRD patterns for LMOns@CC electrode in adsorption-desorption process.

3.4 Selective extraction of Li^+ ions by the LMOns@CC electrode

To extract Li^+ ions from natural salt lake brine, separation of Mg^{2+} and Li^+ ions is a key challenge since the ion radii of Mg^{2+} (72 pm) and Li^+ (76 pm) ions are very close.[19] Therefore, the selective extraction behavior of Li^+ ions under different molar ratios of Mg^{2+}: Li^+ was investigated for the LMOns@CC electrode. The different molar ratios of Mg^{2+}: Li^+ were set to be 1:1, 2:1, 5:1, 10:1, and 20:1, where "1" denoted a

concentration of 20 mmol L^{-1} ions. As seen from **Figure 7a**, when the molar ratio was 1:1, the electrosorption capacity of Mg^{2+} and Li^{+} was 0.87 and 4.34 mmol g^{-1}, respectively. With the increase of Mg^{2+} ion concentration, the electrosorption capability of Li^{+} was decreased, indicating that higher Mg^{2+} ions concentration possesses a certain interference effect on the selective extraction of Li^{+} ions. At the highest molar ratio of 20:1, the lithium extraction capacity was suppressed to 0.84 mmol g^{-1} with the high Mg^{2+} ions capacity of 10.13 mmol g^{-1}. Generally, one key indicator, separation factor ($\alpha_{Mg^{2+}}^{Li^{+}}$), can intuitively determine the potentiality of selective lithium extraction potential for the electrode materials. As shown in **Figure 7b**, $\alpha_{Mg^{2+}}^{Li^{+}}$ increased from 5.5 to 7.48 from the molar ratio increasing from 1:1 to 5:1. Due to the overly high molar ratios of Mg^{2+}, the separation factor was decreased but always far exceeded 1 at the molar ratios of 10:1 and 20:1, still revealing the great potential in selective extraction of lithium ions from brine with a range of Mg/Li ratios.

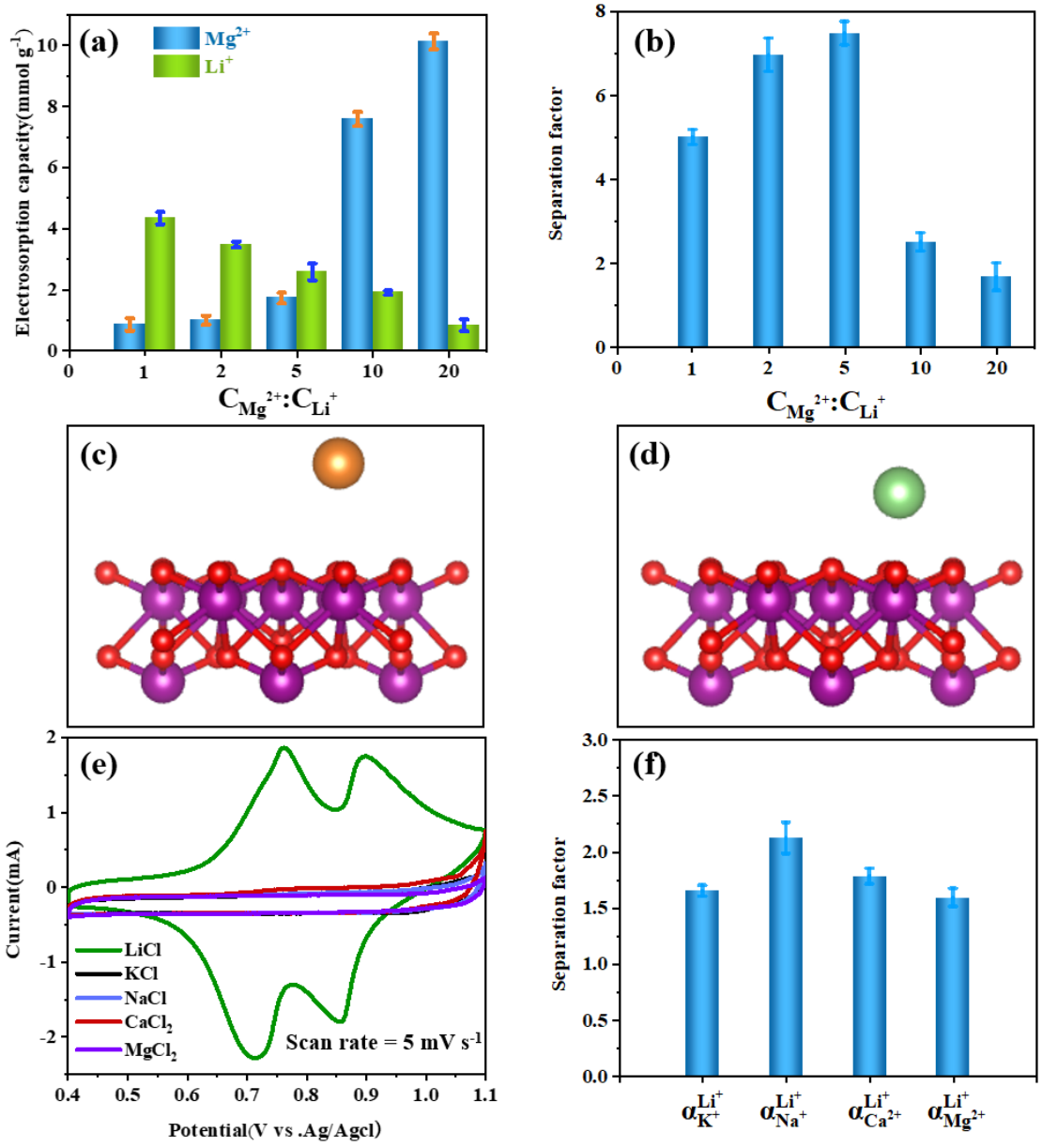

Figure 7. a) Electrosorption capacity of LMOns@CC electrodes under different molar ratios of Mg^{2+}: Li^{+}; b) Separation factor of LMOns@CC electrodes under different molar ratios of Mg^{2+}: Li^{+}; c) Adsorption energy of Mg^{2+} ion on the LMOns@CC electrodes; d) Adsorption energy of Li^{+} ion on the LMOns@CC electrodes; e) CV curve of different electrolyte solution; f) Separation factor of LMOns@CC electrodes in the natural Tibet salt lake brine.

Furthermore, the binding energies (ΔE_a) of λ-MnO_2 to the Mg^{2+} and Li^+ ions were also calculated by using first-principal calculations via CASTEP to determine the process of selective electrosorption. The adsorption models, i.e., Mg^{2+} and Li^+ ions adsorbed on (111) plane of λ-MnO_2, were used by inserting Mg^{2+} and Li^+ atom onto the surface models of the electrode materials and applying the geometric structure optimization (**Figure 7c-d**). The adsorption energy was determined to be ΔE_a = -0.55 and -2.90 eV for Mg^{2+} and Li^+ respectively, based on the results of the geometry optimization. Strong interactions between λ-MnO_2 and the Li^+ atom is indicated by the greatest negative value of the binding energy of the Li^+ atom. This can be attributed to that Li^+ is to be embedded into λ-MnO_2 lattice (specific Faradic behavior), and magnesium Mg^{2+} can only be adsorbed on the surface of λ-MnO_2 (electric double layers).

For a clearer understanding of this selective behavior, the CV test in corresponding single-ion and binary electrolytes was used to trace the origin of selectivity. It found that the two pairs of redox peaks only exist in 0.5 M LiCl solution. However, no peaks appeared in NaCl, KCl, $CaCl_2$, and $MgCl_2$ aqueous electrolytes with the same ion strength (**Figure 7e**). Meanwhile, the integrated area of the whole CV curve for LiCl was also higher than those for other electrolytes. These results reveal that LMOns@CC exhibits remarkable Li^+ ions selectivity, while other ions with larger ion radii (Na^+, K^+, and Ca^{2+}) or higher hydration energy (Mg^{2+}) may be more challenging to intercalate into the $LiMn_2O_4$ crystals. Besides the main challenge of Mg^{2+}, the influence of other alkaline metal ions, including Na^+, K^+, Ca^{2+}, and other cationic ions with low

concentration, is also vital. Therefore, the natural salt lake brine (Baqiancuo, Tibet, China, **Table S1**) was further used to investigate the selective Li^+ extraction performance of LMOns@CC electrodes. **Figure 7f** shows that the LMOns@CC electrode still showed good selectivity ($\alpha_{K^+}^{Li^+}$ = 1.65, $\alpha_{Na^+}^{Li^+}$ = 2.21, $\alpha_{Ca^{2+}}^{Li^+}$ = 1.78, $\alpha_{Mg^{2+}}^{Li^+}$ = 1.59) in the natural salt lake brine. It further indicates that LMOns@CC electrodes exhibit excellent lithium selective adsorption performance in complex symbiotic cationic environments.

3.6 Cycle stability valuation of the LMOns@CC electrodes

The main problem in the practical application of LMO electrodes is cycle stability. It has been stated that Jahn–Teller distortion and Mn dissolution are to blame for the poor cycle stability of LMO.[47, 48] To reveal the superiority of the LMOns@CC electrode, it is compared with the commercial LMO (CLMO) under the same experimental conditions. To ensure the consistency of the experiment, a uniform CLMO slurry was applied to a carbon cloth of the same size. The slurry is made by mixing CLMO, Ketjen black, and PVDF with a mass ratio of 8:1:1 and stirring for 24 hours according to our previous work.[49] In the current work, the recyclability of LMOns@CC and CLMO electrodes was evaluated by cyclic discharge/charge in 150 mg L^{-1} LiCl solution via the Lanhe testing system. **Figure 8a** shows the immediate conductivity variations of the solution during the electrosorption process by the LMOns@CC electrode. It can be seen that the conductivity remained stable during ten cycles of adsorption-desorption, and the capacity retention of 97.4% was achieved for the LMOns@CC electrode within the 10 cycles, indicating good cycling stability.

Figure 8b shows the continuous current change during the cycles, in which the current trend in each cycle remains unchanged. In contrast, the cycling stability of the CLMO electrode was worse than LMOns@CC during electrosorption-desorption cycles. Meanwhile, the conductivity increases gradually due to the dissolution of Mn. Therefore, the Li^+ electrosorption capacity of the CLMO electrode only retained 76.6% in **Figure 8c**. **Figure 8d** illustrates the continuous current change of CLMO during the 10 cycles under the same conditions. By contrast, the current generated by the CLMO electrode is obviously smaller than that of the LMOns@CC electrode for the lithium adsorption process. The comparison of charge efficiency between LMOns@CC and CLMO electrodes was shown in **Figure S8**. It is obvious that the charge efficiency of the LMOns@CC electrode (99.66%) is higher than that of CLMO (94.56%) in the tenth cycles. The reason for this difference is attributed to the following two aspects: First, the use of binders leads to a decrease in conductivity and reduce the hydrophilicity of the electrode. Second, this nanostructure can effectively improve the utilization of electrode materials. **Figure 8e** shows that the manganese dissolution ratio of the LMOns@CC electrode is 0.35%, which is four-time lower than 1.77% for the CLMO electrode after 10 cycles. It indicated that the nanosheet structure of the LMOns@CC electrode could significantly inhibit the manganese dissolution by the stability of the structure.[50] Moreover, a 2D nanosheet structure can effectively prevent manganese dissolution caused by lattice expansion. The SEM image of LMOns@CC showed that the morphology of the 2D nanosheet is still maintained after 10 cycles (**Figure 8f**). In addition, the XRD patterns of LMOns@CC electrodes before and after cycling were

similar, indicating the crystal structure stability of LMO in the LMOns@CC electrode (**Figure S9**). The exceptional cycles stability and low manganese dissolution ratio of the LMOns@CC electrode can be ascribed to their distinctive nanostructure in following ways: First, this electrode has remarkable cycling stability due to its high crystallinity, nanometer size, and mesoporous nanosheet structure, which considerably increase the stability of the electrode in process of electrosorption-desorption cycles. Second, the special structure and the existence of small particles can accelerate the ions into the electrode, so that the ions can spread rapidly with a shorter diffusion path, and the utilization rate of active materials can be further improved.

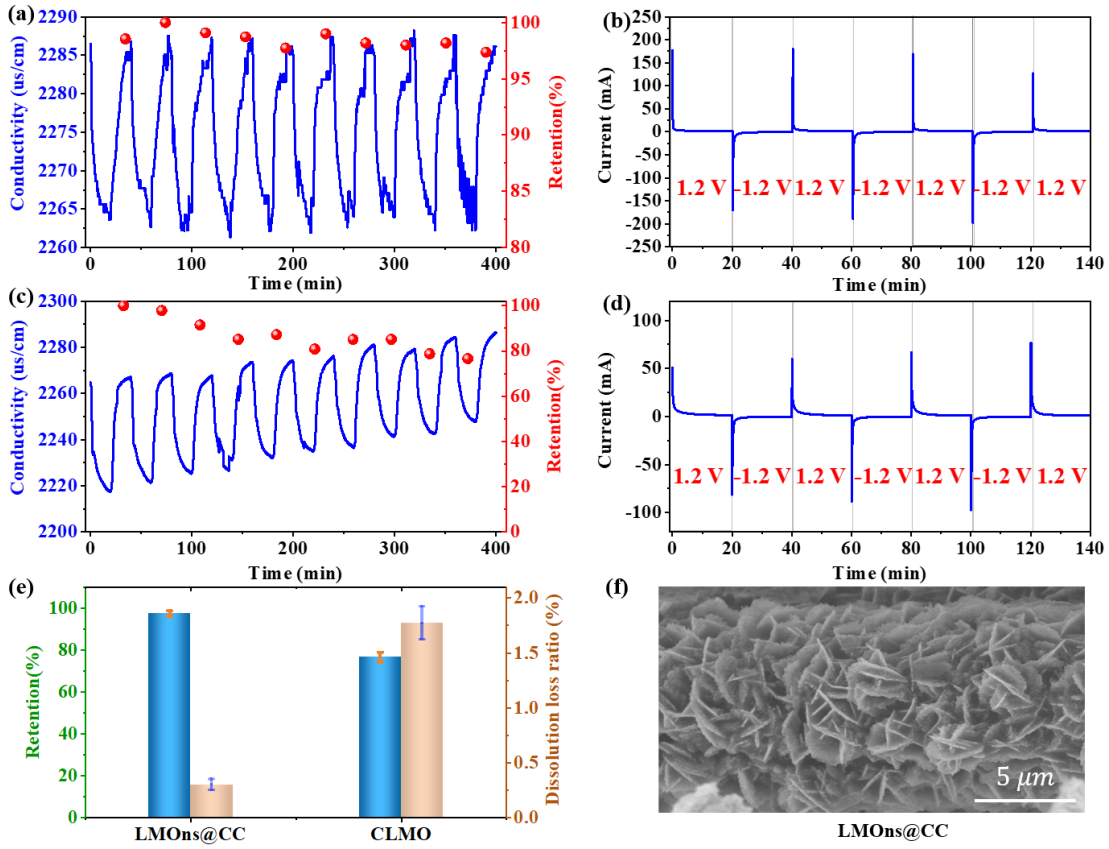

Figure 8. a) Immediate conductivity variations of 150 mg L^{-1} LiCl solution by the LMOns@CC electrode; b) Immediate current-voltage changes of the LMOns@CC

electrode; c) Immediate conductivity changes of 150 mg L^{-1} LiCl solution by the CLMO electrode; d) Immediate current-voltage changes of the CLMO electrode; e) Manganese dissolution and retention ratio of the LMOns@CC and CLMO electrode after ten cycles; f) SEM image of LMOns@CC electrode after ten cycles.

Table 1 summarizes the differences between the current study and earlier efforts in the reported literatures in terms of electrosorption capacitance, manganese dissolution ratio, and cycle stability. The electrosorption capacitance of LMOns@CC is superior to that of the most reported materials.[31, 43] The excellent electrosorption capacity is attributed to the more active sites of LMO electrodes with binder-free 2D order array nanosheet structures constructed by small particle sizes. These features can speed up electrolyte penetration into the electrode and enable fast ion diffusion with significantly shorter diffusion lengths. Furthermore, the LMOns@CC electrode could maintain $\approx$ 97.4% of adsorption capacity after 10 cycles, superior to that of the most of reported works.[23] The mesoporous nanosheet structure endows this electrode with much better structural stability during the cycling process, which is largely responsible for its exceptional cycling stability and low manganese dissolution ratio. It is noteworthy that this nanosheet structure can effectively suppress the lattice expansion caused by ion absorption and desorption. These results demonstrated that the LMOns@CC electrode could be a highly competitive candidate for lithium extraction from brines and seawater.

Table 1. Comparison of electrosorption performance between LMOns@CC//AC and other reported works in literatures.

Electrode materials	Equilibrium Time (min)	Q (mmol/g)	Retention/ cycles	Manganese dissolution	AEM	Ref.
$LN_{0.5}M_{1.5}O$//AC	30	0.26	86%/100	-	Yes	[30]
LMO//Zn	300	0.71	73%/100	-	Yes	[46]
NCM//Ag	20	1.56	-	-	No	[44]
CNT-s-LMO//AC	60	1.6	90%/100	0.15%	Yes	[31]
LMO//PANI	216	3.39	70.8%/200	-	No	[42]
PDA-C@HMO//AC	60	9.45	90.2%/10	7.5%	Yes	[23]
LMO film//Ag	60	3.76	82.3%/100	-	No	[43]
Meso-LMO@GF	10	3.77	90.4%/20	2.17%	Yes	[15]
LMOns@CC//AC	60	4.71	97.4%/10	0.35%	Yes	This work

3. Conclusion

In summary, a three-step process including the production of cathodic deposition $Mn(OH)_2$@CC, self-oxidation MOns@CC, and *in-situ* lithiation under hydrothermal conditions was used to produce the binder-free $LiMn_2O_4$ nanosheets (LMOns) electrodes on carbon cloth (CC) substrates. The as-prepared binder-free LMOns@CC electrode has good electron/ proton transfer rates, high specific capacity, and excellent cyclic stability due to the highly ordered two-dimensional mesoporous nanosheet structure on the carbon cloth substrates. The hybrid LMOns@CC//AC cell has a high electrosorption capacity of 4.71 mmol g^{-1} at 1.2 V, which is an advantage over other reported materials in previous works. Meanwhile, the performance of the LMOns@CC electrode remained up to 97.4%, and the manganese dissolution ratio was only 0.35%

after 10 electrosorption-desorption cycles. At a higher Mg^{2+}/Li^{+} molar ratio solution, the separation factor was achieved to 7.48 and the electrosorption performance is basically unchanged after 100 cycles. Furthermore, the DFT calculation demonstrated that the selective extraction of Li^{+} ion is attributed to the large adsorption energy between Li^{+} ion and the LMOns@CC electrode. The binder-free electrode material proposed in this study will help accelerate the development of the field of lithium extraction with high adsorption capacity and good cycle, and provide a beneficial direction and solution.

4. Experimental Section

Preparation of the binder-free LMOns@CC electrode: A feasible three-step strategy, including cathode deposition, self-oxidation, and lithiation, was used to prepare the binder-free LMOns@CC electrode. Firstly, the carbon cloth substrates (5×4 cm^2) were pretreated via the plasma device for 15 minutes on the power of 80 W to enhance the hydrophilicity of carbon cloth. Then, the cathode deposition was conducted in a mixed electrolyte with 15 mM manganese acetate and 15 mM sodium sulfate by a three-electrode electrochemical system assembled with a CC substrate as the cathode, a graphite plate (5×5 cm^2) as the anode, and an Ag/AgCl as reference electrode **(Figure S1)**. After using an I-t curve of –1.4 V vs. Ag/AgCl for 2500 s, $Mn(OH)_2$ was deposited on a CC substrate, followed by adequate washing with deionized water. Subsequently, the $Mn(OH)_2$@CC was oxidized to stable Mn_3O_4@CC overnight at room temperature. The prepared Mn_3O_4@CC was immersed in 30 mL of 20 mM LiOH solution and transferred to 50 mL of Teflon-lined stainless steel for the hydrothermal process at

220 °C for 17 h. The LMOns@CC were recovered by washing with deionized water and drying in an oven at 80 °C.

The CDI performances of binder-free LMOns@CC electrode: Before the LMOns@CC was used for the CDI test, the pretreatment to produce the delithiated L_{1-x}MOns@CC electrode was necessary. The L_{1-x}MOns electrode was prepared by electro-desorption under the voltage of -1.2 V in a 20 mM NaCl solution with a pH of 2–3 for 1 h, in which the LMOns@CC electrode was used as an anode, activated carbon (AC) as a cathode, and a separated anion-exchange membrane was assembled in an HCDI cell (**Figure S2**).

The active area of the LMOns@CC electrode used in the CDI experiment was about 4×4 cm^2, and the load mass of LMOns@CC was about 14 mg. The adsorption experiments of Li^+ ions were carried out under different applied voltages (0–1.2 V) and different concentrations of Li^+ ions (10, 30, 50, 100, 150, and 200 mg L^{-1}). Meanwhile, Li^+ selective adsorption experiments were conducted in the mixture solution of Li^+ and Mg^{2+} ions with different molar ratios and natural brine from Tibet salt lake (Baqiancuo, Tibet, China). In all HCDI experiments, the flow rate was 15 mL min^{-1}, and the volume of solution was 50 mL. A reverse electric field was used to carry out the desorption process of Li^+ ions. The concentration of cation in the solution was determined by an inductively coupled plasma optical emission spectrometer (ICP-OES, ICP 7400, Thermo Fisher Scientific, USA).

Declaration of Competing Interest

The authors declare that they have no known competing financial interests or personal relationships that could have appeared to influence the work reported in this paper.

Supporting Information

Supporting Information is available from the Wiley Online Library or from the author.

Acknowledgment

This work was financially supported by National Key R&D Program of China (2022YFC2904303), The Open Project of Salt Lake Chemical Engineering Research Complex, Qinghai University (2023-DXSSKF-07), the National Natural Science Foundation of China (Grant No. 51872291), the Key Research and Development Projects of Anhui Province (Grant No.202104a06020028).

Received: ((will be filled in by the editorial staff))
Revised: ((will be filled in by the editorial staff))
Published online: ((will be filled in by the editorial staff))

References

1. Xiong, Y.; Zhou, J.; Lu, P.; Yin, J.; Wang, Y.; Fan, Z., *Matter* **2022,** *5* (6), 1760-1791.
2. Lang, J.; Qi, L.; Luo, Y.; Wu, H., *Energy Storage Materials* **2017,** *7*, 115-129.
3. Zavahir, S.; Elmakki, T.; Gulied, M.; Ahmad, Z.; Al-Sulaiti, L.; Shon, H. K.; Chen, Y.; Park, H.; Batchelor, B.; Han, D. S., *Desalination* **2021,** *500*, 114883.
4. Martin, G.; Rentsch, L.; Höck, M.; Bertau, M., *Energy Storage Materials* **2017,** *6*, 171-179.
5. Grosjean, C.; Miranda, P. H.; Perrin, M.; Poggi, P., *Renewable and Sustainable Energy Reviews* **2012,** *16* (3), 1735-1744.
6. Jiang, C.; Chen, B.; Xu, Z.; Li, X.; Wang, Y.; Ge, L.; Xu, T., *AIChE Journal* **2022,** *68* (6), e17710.
7. Xu, P.; Hong, J.; Qian, X.; Xu, Z.; Xia, H.; Tao, X.; Xu, Z.; Ni, Q.-Q., *Journal of Materials Science* **2020,** *56* (1), 16-63.
8. Sun, Y.; Wang, Q.; Wang, Y.; Yun, R.; Xiang, X., *Separation and Purification Technology* **2021,** *256*, 117807.
9. Zhang, Y.; Hu, Y.; Wang, L.; Sun, W., *Minerals Engineering* **2019,** *139*, 105868.

10. Zhao, C.; Zhang, Y.; Cao, H.; Zheng, X.; Van Gerven, T.; Hu, Y.; Sun, Z., *Ultrason Sonochem* **2019,** *52*, 484-492.
11. He, L.; Xu, W.; Song, Y.; Liu, X.; Zhao, Z., *Separation and Purification Technology* **2017,** *187*, 214-220.
12. Hanada, T.; Goto, M., *ACS Sustainable Chemistry & Engineering* **2021,** *9* (5), 2152-2160.
13. Zhang, L.; Li, J.; Liu, R.; Zhou, Y.; Zhang, Y.; Ji, L.; Li, L., *Journal of Molecular Liquids* **2022,** *362*, 119667.
14. Zhang, L.; Li, L.; Rui, H.; Shi, D.; Peng, X.; Ji, L.; Song, X., *J Hazard Mater* **2020,** *398*, 122840.
15. Mu, Y.; Zhang, C.; Zhang, W.; Wang, Y., *Desalination* **2021,** *511*, 115112.
16. Guo, Z.-Y.; Ji, Z.-Y.; Wang, J.; Guo, X.-F.; Liang, J.-S., *Desalination* **2022,** *533*, 115767.
17. Zhang, J.; Su, W.; Yi, B.; Guo, Y.; Deng, T.; Yu, X., *Chemical Engineering Journal* **2023,** *454*, 140416.
18. Xu, S.; Song, J.; Bi, Q.; Chen, Q.; Zhang, W.-M.; Qian, Z.; Zhang, L.; Xu, S.; Tang, N.; He, T., *Journal of Membrane Science* **2021,** *635*, 119441.
19. Zhang, Y.; Wang, L.; Sun, W.; Hu, Y.; Tang, H., *Journal of Industrial and Engineering Chemistry* **2020,** *81*, 7-23.
20. Shi, W.; Liu, X.; Ye, C.; Cao, X.; Gao, C.; Shen, J., *Separation and Purification Technology* **2019,** *210*, 885-890.
21. Li, X.; Mo, Y.; Qing, W.; Shao, S.; Tang, C. Y.; Li, J., *Journal of Membrane Science* **2019,** *591*, 117317.
22. Du, X.; Guan, G.; Li, X.; Jagadale, A. D.; Ma, X.; Wang, Z.; Hao, X.; Abudula, A., *Journal of Materials Chemistry A* **2016,** *4* (36), 13989-13996.
23. Wang, Y.; Zhang, J.; Cheng, Z.; Xiang, X., *ACS Sustainable Chemistry & Engineering* **2022,** *10* (27), 8970-8979.
24. Zhao, M.-Y.; Ji, Z.-Y.; Zhang, Y.-G.; Guo, Z.-Y.; Zhao, Y.-Y.; Liu, J.; Yuan, J.-S., *Electrochimica Acta* **2017,** *252*, 350-361.
25. Moazeni, M.; Hajipour, H.; Askari, M.; Nusheh, M., *Materials Research Bulletin* **2015,** *61*, 70-75.
26. He, L.; Xu, W.; Song, Y.; Luo, Y.; Liu, X.; Zhao, Z., *Glob Chall* **2018,** *2* (2), 1700079.
27. Xiong, J.; He, L.; Liu, D.; Xu, W.; Zhao, Z., *Desalination* **2021,** *520*, 115326.
28. Yuan, J.-S.; Yin, H.-B.; Ji, Z.-Y.; Deng, H.-N., *Industrial & Engineering Chemistry Research* **2014,** *53* (23), 9889-9896.
29. Zhou, G.; Chen, L.; Li, X.; Luo, G.; Yu, Z.; Yin, J.; Fan, L.; Chao, Y.; Jiang, L.; Zhu, W., *Green Energy & Environment* **2022,** *8* (4), 1081-1090.
30. Shang, X.; Hu, B.; Nie, P.; Shi, W.; Hussain, T.; Liu, J., *Separation and Purification Technology* **2021,** *258*, 118009.
31. Shang, X.; Liu, J.; Hu, B.; Nie, P.; Yang, J.; Zhang, B.; Wang, Y.; Zhan, F.; Qiu, J., *Small Methods* **2022,** *6* (7), e2200508.
32. Wen, X.; Zhao, M.; Zhang, M.; Fan, X.; Zhang, D., *ACS Sustainable Chemistry & Engineering* **2019,** *8* (2), 1268-1275.

33. Talebi, M.; Ahadian, M. M.; Shahrokhian, S., *Diamond and Related Materials* **2021,** *120*, 108612.
34. Wen, X.; Zhao, M.; Zhao, Z.; Ma, X.; Ye, M., *ACS Sustainable Chemistry & Engineering* **2020,** *8* (19), 7335-7342.
35. Cai, Y.; Zhang, L.; Fang, R.; Wang, Y.; Wang, J., *Separation and Purification Technology* **2022,** *292*, 121019.
36. Wei Xiao, H. X., Jerry-Ying-Hsi Fuh, and Li Lu, *Journal of The Electrochemical Society* **2009,** *156* (7), A627-A633.
37. Huang, Y.; Dong, Y.; Li, S.; Lee, J.; Wang, C.; Zhu, Z.; Xue, W.; Li, Y.; Li, J., *Advanced Energy Materials* **2020,** *11* (2), 2000997.
38. Gao, Y.; Xu, Y.; Xiang, S.; Zhang, X.; Li, Z.; Zhou, H., *Environmental Science: Nano* **2022,** *9* (6), 2051-2060.
39. Xiang, S.; Mao, H.; Geng, W.; Xu, Y.; Zhou, H., *J Hazard Mater* **2022,** *431*, 128591.
40. Xu, W.; He, L.; Zhao, Z., *Desalination* **2021,** *503*, 114935.
41. Zhao, X.; Li, G.; Feng, M.; Wang, Y., *Electrochimica Acta* **2020,** *331*, 135285.
42. Zhao, A.; Liu, J.; Ai, X.; Yang, H.; Cao, Y., *ChemSusChem* **2019,** *12* (7), 1361-1367.
43. Xu, X.; Zhou, Y.; Feng, Z.; Kahn, N. U.; Haq Khan, Z. U.; Tang, Y.; Sun, Y.; Wan, P.; Chen, Y.; Fan, M., *Chempluschem* **2018,** *83* (6), 521-528.
44. Lawagon, C. P.; Nisola, G. M.; Cuevas, R. A. I.; Kim, H.; Lee, S.-P.; Chung, W.-J., *Chemical Engineering Journal* **2018,** *348*, 1000-1011.
45. Kim, S.; Kim, M.; Woo, S.; Kang, H.; Kim, S., *Current Applied Physics* **2018,** *18* (3), 340-344.
46. Kim, S.; Lee, J.; Kim, S.; Kim, S.; Yoon, J., *Energy Technology* **2018,** *6* (2), 340-344.
47. Yu, X.; Deng, J.; Yang, X.; Li, J.; Huang, Z.-H.; Li, B.; Kang, F., *Nano Energy* **2020,** *67*, 104256.
48. Xu, H.; Zhang, H.; Zhao, S.; Huang, W.; Qu, Z.; Yan, N., *Chemical Engineering Journal* **2016,** *299*, 142-149.
49. Xu, Y.; Xiang, S.; Zhang, X.; Zhou, H.; Zhang, H., *J Hazard Mater* **2022,** *439*, 129575.
50. X. Q. Yang, X. S., S. J. Lee,J. McBreen, S. Mukerjee,M. L. Daroux,and X. K. Xing, *Electrochemical and Solid-State Letters* **1999,** *2(4)*, 157-160.

This work introduces a three-step strategy including electrochemical cathode deposition, self-oxidation, and hydrothermal reaction to construct binder-free electrodes by in-situ growth of the $LiMn_2O_4$ materials with highly ordered hierarchical nanostructures on a highly flexible conductive carbon cloth substrate as a binder-free cathode in a hybrid capacitive deionization cell for selectively extracting lithium from salt-lake brine.

G. Ma, Y. Xu, A. Cai,* H. Mao, X. Zhang, D. M. Shin, L. Wang, H. Zhou*

Binder-free $LiMn_2O_4$ Nanosheets on Carbon Cloth for Selective Lithium Extraction from Brine via Capacitive Deionization